

Bayesian inference and uncertainty propagation using efficient fractional-order viscoelastic models for dielectric elastomers

Paul R Miles¹ , Graham T Pash^{1,2}, Ralph C Smith²  and William S Oates³

Journal of Intelligent Material Systems and Structures

2021, Vol. 32(4) 486–496

© The Author(s) 2020

Article reuse guidelines:

sagepub.com/journals-permissions

DOI: 10.1177/1045389X20969847

journals.sagepub.com/home/jim



Abstract

Dielectric elastomers are employed for a wide variety of adaptive structures. Many of these soft elastomers exhibit significant rate-dependencies in their response. Accurately quantifying this viscoelastic behavior is non-trivial and in many cases a nonlinear modeling framework is required. Fractional-order operators have been applied to modeling viscoelastic behavior for many years, and recent research has shown fractional-order methods to be effective for nonlinear frameworks. This implementation can become computationally expensive to achieve an accurate approximation of the fractional-order derivative. Accurate estimation of the elastomer's viscoelastic behavior to quantify parameter uncertainty motivates the use of Markov Chain Monte Carlo (MCMC) methods. Since MCMC is a sampling based method, requiring many model evaluations, efficient estimation of the fractional derivative operator is crucial. In this paper, we demonstrate the effectiveness of using quadrature techniques to approximate the Riemann–Liouville definition for fractional derivatives in the context of estimating the uncertainty of a nonlinear viscoelastic model. We also demonstrate the use of parameter subset selection techniques to isolate parameters that are identifiable in the sense that they are uniquely determined by measured data. For those identifiable parameters, we employ Bayesian inference to compute posterior distributions for parameters. Finally, we propagate parameter uncertainties through the models to compute prediction intervals for quantities of interest.

Keywords

Fractional derivative, Riemann–Liouville, dielectric elastomers, viscoelasticity, Bayesian inference, uncertainty propagation

1. Introduction

Models employing fractional-order derivatives have become increasingly popular in a wide variety of scientific disciplines, and it has been found particularly useful in modeling viscoelasticity in soft elastomers (Mashayekhi et al., 2018). The rate-dependent hysteresis responses of viscoelastic materials pose significant challenges for traditional integer-order models. Fractional-order models on the other hand are adept at modeling this rate-dependent phenomenon due to the non-local behavior of the fractional-order operators. Given the current popularity of fractional-order models, efficient approaches for approximating these mathematical operators is extremely important. This can be challenging, as many fractional derivatives require extended numerical precision to achieve reasonable accuracy.

There are various definitions for fractional derivatives, such as Riemann–Liouville, Caputo, and Grünwald–Letnikov (Podlubny, 1998). In this investigation, we present numerical methods for approximating the Riemann–Liouville definition for fractional derivative in the regime where the fractional-order is in the interval $\alpha \in [0, 1)$. This interval is of particular

¹Department of Mathematics, North Carolina State University, Raleigh, NC, USA

²Department of Mechanical Engineering, North Carolina State University Raleigh, NC, USA

³Department of Mechanical Engineering, Florida A&M University and Florida State University, Tallahassee, FL, USA

Corresponding author:

Ralph C. Smith, Department of Mathematics, North Carolina State University, P.O. Box 8205, Raleigh, NC 27695, USA.

Email: rsmith@ncsu.edu

interest in viscoelastic domains because this fractional-order combines both zero-order elastic and first-order viscous effects. We discuss the Grünwald–Letnikov definition since this method is often used in situations where only discrete data is available, making it the preferred definition when numerical approximation is required. The Grünwald–Letnikov is used as a baseline to assess the accuracy of several of our numerical methods for the Riemann–Liouville definition.

To fully assess the robustness of these fractional-order models requires estimation of model parameter uncertainty in order to provide greater confidence in the models predictive ability. By taking a Bayesian approach, we can efficiently estimate the uncertainty of fractional-order viscoelastic models. Furthermore, by utilizing sensitivity analysis, we can reduce the parameter space to be estimated, thereby simplifying the task of model calibration. From our statistical framework, propagation of uncertainty provides credible and prediction intervals, which help quantify the overall confidence in the model.

2. Model framework

For our application, the quantity of interest (QoI) is the nominal stress (Holzapfel, 2000). We utilize a set of energy density functions which describe the hyperelastic and viscoelastic phenomena observed in the material. These energy functions relate to the nominal stress to its work conjugate variable, the deformation gradient (Holzapfel, 2000). The energy functions presented here include thermal effects; however, in our analysis and model validation we assume isothermal deformation. For more details regarding the specific models used here, the reader is referred to Miles et al. (2015) and Mashayekhi et al. (2018). For clarity, we summarize key model equations.

The total free energy density is given by $\hat{\psi} = \psi - p(J - 1)$, where J is the determinant of the deformation gradient which is constrained to be one by the hydrostatic pressure p such that the deformation is incompressible.

The free energy (ψ) within this equation includes

$$\psi = \psi_{\infty}(F_{iK}, \Theta) + Y(F_{iK}, \Theta, \xi_{iK}^{\nu}) \quad (1)$$

which is decomposed into two terms: (1) ψ_{∞} is the reversible, hyperelastic free energy function that depends on the deformation gradient F_{iK} and temperature Θ , and (2) Y is an energy function that additionally depends on a set of internal state variables, ξ_{iK}^{ν} , $\nu = 1, \dots, n$. These internal states contribute to the dissipation observed during rate-dependent deformation. In all analyses presented here, we let $\nu = 1$ as done in prior model validation (Mashayekhi et al., 2018; Miles et al., 2015).

For the reversible energy term, we consider the non-affine function (Davidson and Goulbourne, 2013):

$$\psi_{\infty} = \frac{1}{6} G_c I_1 - G_c \lambda_{\max}^2 \ln(3\lambda_{\max}^2 - I_1) + G_e \sum_j \left(\lambda_j + \frac{1}{\lambda_j} \right), \quad (2)$$

where G_c is the crosslink network modulus, G_e is the plateau modulus which describes entanglement effects, λ_{\max} is the maximum stretch of the effective affine tube, and $I_1 = \lambda_i \lambda_i$ is the first stretch invariant where summation on i is implied. We note that the stretch (λ_i) is a measure of deformation and corresponds to the principal components of the deformation gradient (F_{iK}). Since we are only considering uniaxial loading, stretch is a sufficient description of the deformation.

For the purpose of our analysis, we employ the following, internal state energy function

$$Y = \frac{1}{2} \gamma \xi_{iK} \xi_{iK} - \beta_{\infty} \frac{\partial \psi_{\infty}}{\partial F_{iK}} \xi_{iK} + \beta_{\infty} \psi_{\infty}. \quad (3)$$

Here β_{∞} and γ are viscoelastic model parameters. This energy function is quadratic in the internal state ξ_{iK}^{ν} which leads to a linear viscoelastic relation. However, the terms proportional to β_{∞} lead to non-linear viscoelasticity behavior since it is proportional to the nonaffine energy function in equation (2) and non-affine stress $s_{iK}^{\infty} = \frac{\partial \psi_{\infty}}{\partial F_{iK}}$. Details describing this viscoelastic modeling framework is given by Holzapfel and Simo (1996). Additional details describing the model derivation, fractional viscoelastic assumptions, and experimental validation can be found in Mashayekhi et al. (2018).

The QoI is the nominal stress,

$$s_{iK} = \frac{\partial \hat{\psi}}{\partial F_{iK}} = \frac{\partial \psi_{\infty}}{\partial F_{iK}} - p J H_{iK} + \frac{\partial Y}{\partial F_{iK}}, \quad (4)$$

which applies equations (1) to (3) to obtain the reversible stresses from the first two terms and the viscoelastic stress from the last term.

The viscoelastic stress given by the last term in equation (4) is explicitly given to highlight how fractional-order time derivatives are introduced within our model. The viscoelastic stress can be described by

$$\frac{\partial Y}{\partial F_{iK}} = \beta_{\infty} \left[s_{iK}^{\infty} - \frac{\partial s_{mN}^{\infty}}{\partial F_{iK}} \left(\frac{1}{\gamma} (\beta_{\infty} s_{mN}^{\infty} - \eta D_t^{\alpha} s_{mN}^{\infty}) \right) \right]. \quad (5)$$

Additional details describing the derivation and the assumptions that go into this equation are described by Mashayekhi et al. (2018). The key relation introduced here is the fractional operator D_t^{α} , where α is the order of the fractional time derivative and η is the viscoelastic

parameter. To obtain this relation, a time rate of change of ξ_{mN} is introduced in a positive definite entropy generation function. This time rate of change of ξ_{mN} is assumed to be proportional to the fractional time rate of change of s_{mN}^∞ which leads to the final term in equation (5). The introduction of this operator still satisfies all thermodynamic requirements of the energy model and positive definite entropy generation. Details regarding fractional derivatives are provided in Section 3.

3. Fractional-order derivatives

As detailed in (Mashayekhi et al., 2018), we make the assumption that the rate of internal state variables is proportional to the local fractional time derivative of the hyperelastic stress to obtain the model detailed in Section 2. This section introduces the fractional derivative operator as well as methods for accurately and efficiently approximating this operator.

Definition 1. The Riemann–Liouville definition for fractional derivatives is

$$D_{RL}^\alpha[f(t)] = \frac{1}{\Gamma(n-\alpha)} \frac{d^n}{dt^n} \int_0^t \frac{f(s)}{(t-s)^{\alpha+1-n}} ds, \quad (6)$$

where $n = [\alpha]$. We will restrict our analysis further by only considering the regime where $\alpha \in [0, 1)$. Therefore $n = 1$, and the definition simplifies to

$$D_{RL}^\alpha[f(t)] = \frac{1}{\Gamma(1-\alpha)} \frac{d}{dt} \int_0^t \frac{f(s)}{(t-s)^\alpha} ds. \quad (7)$$

Definition 2. The Grünwald–Letnikov fractional derivative of order α is defined as

$$D_G^\alpha[f(t)] = \lim_{h \rightarrow 0} \frac{1}{h^\alpha} \sum_{0 \leq m < \infty} (-1)^m \binom{\alpha}{m} f(t-mh). \quad (8)$$

Lemma 1. (Oldham and Spanier, 1974): If $f(t)$ is $(n-1)$ times differentiable in $[0, b]$ and the n^{th} derivative of $f(t)$ is integrable in $[0, b]$. Then, for every $n-1 < \alpha < n$ we have

$$D_G^\alpha[f(t)] = D_{RL}^\alpha[f(t)], \quad 0 \leq t \leq b. \quad (9)$$

Our goal is to approximate the value of the Riemann–Liouville fractional derivative operator defined in equation (7), where $\alpha \in [0, 1)$. To facilitate our numerical approximations, we define the term

$$F[t] = \int_{t_0}^t (t-s)^{-\alpha} f(s) ds. \quad (10)$$

Note that equation (10) is the integral portion of the fractional derivative in equation (7). We can evaluate

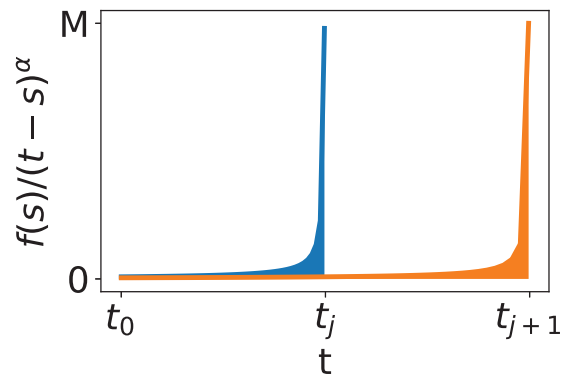


Figure 1. The integral approximations must account for the boundary singularity at the upper limit of integration.

$F(t)$ at any time and observe that equation (7) can be equivalently expressed as

$$D_{RL}^\alpha[f(t)] = \chi \frac{d}{dt} F[t] \approx \chi \frac{F(t_{j+1}) - F(t_j)}{t_{j+1} - t_j}, \quad (11)$$

where $\chi = \Gamma(1-\alpha)^{-1}$. This approach to approximating the Riemann–Liouville fractional derivative comes from Atangana and Gómez-Aguilar (2017). Here we extend their work by presenting various approaches to efficiently evaluate the integral expression in equation (10). Figure 1 illustrates the issues associated with approximating the Riemann–Liouville fractional derivative. We approximate the area under each curve, where the distance between the upper limits is separated by some finite time. By taking the difference in areas and dividing by the finite step length, we can approximate the Riemann–Liouville fractional derivative. There is a singularity at the upper limit of integration, which will require special quadrature methods as outlined below.

3.1. Quadrature methods

In general, all quadrature methods can be represented as

$$\int_{t_0}^{t_n} f(x) dx \approx \sum_{i=1}^N f(x_i) w_i, \quad (12)$$

where x_i and w_i are the quadrature nodes and weights. To present a consistent notation with respect to equation (10), we instead use the following quadrature representation,

$$\int_{t_0}^{t_n} (t_n - s)^{-\alpha} f(s) ds \approx \sum_{i=1}^N f(x_i) w_i \quad (13)$$

where the singularity is now accounted for in the weights, w_i .

3.2. Riemann-sum

As presented in Atangana and Gómez-Aguilar (2017), the two integral expressions, $F(t_{j+1})$ and $F(t_j)$, can be approximated using the following methodology. If one assumes that the function $f(t)$ behaves in a piecewise smooth manner for each sub-interval of integration, one can then factor it out of the integral. By taking reasonably small intervals, one can approximate $f(t)$ as being constant, typically by evaluating the function at the average of the end points of the interval. Mathematically, for the integral $F(t_n)$, this leads to the following approximation

$$F(t_n) = \int_{t_0}^{t_n} (t_n - s)^{-\alpha} f(s) ds \approx \sum_{k=0}^{n-1} f(x_k) w_k, \quad (14)$$

where

$$x_k = \frac{t_{k+1} + t_k}{2}, \quad w_k = \int_{t_k}^{t_{k+1}} (t_n - s)^{-\alpha} ds. \quad (15)$$

The weights can be computed analytically because we are assuming that the fractional-order is less than 1. Therefore, we can reduce the weights into an explicit expression

$$\begin{aligned} w_k &= \frac{-1}{1-\alpha} (t_n - s)^{1-\alpha} \Big|_{s=t_k}^{t_{k+1}} \\ &= \frac{-1}{1-\alpha} [(t_n - t_{k+1})^{1-\alpha} - (t_n - t_k)^{1-\alpha}]. \end{aligned} \quad (16)$$

For the present analysis, we typically define the evaluation times to be a uniform grid from t_0 to t_n .

It should be noted that this approach effectively accounts for the singularity in the upper limit of integration seen in equation (10). However, if $f(t)$ were to vary significantly with small time steps, this method may not be accurate. Assuming that $f(t)$ is approximately a piecewise constant in each sub-interval may necessitate the use of extremely dense grids to maintain accuracy.

3.3. Gauss–Laguerre

An alternative quadrature approach for integrals with boundary singularities is the Gauss–Laguerre method (Griebel and Oettershagen, 2014). To modify this method for the Riemann–Liouville fractional derivative, we must map the Gauss–Laguerre quadrature domain from $[0, \infty]$ to $[0, 1]$. This is accomplished via the u -substitution:

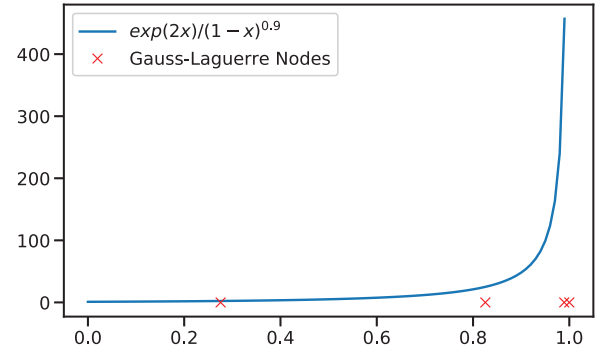


Figure 2. Four-point Gauss–Laguerre quadrature nodes demonstrated for kernel $\exp(2t)/(1-t)^{0.9}$ on domain $t \in [0, 1]$.

$$\underbrace{\int_{t_0}^{t_n} \frac{f(s)}{(t_n - s)^\alpha} ds}_{\text{Substitute } u = \frac{s - t_0}{t_n - t_0}; ds = (t_n - t_0) du; u(s=t_0) = 0, u(s=t_n) = 1} = \int_0^1 \frac{f((t_n - t_0)u + t_0)}{(t_n - t_0)^{1-\alpha} (1-u)^\alpha} du. \quad (17)$$

The expression in equation (17) can be approximated via the quadrature

$$F(t_n) \approx \sum_{k=1}^n f(x_k) w_k, \quad (18)$$

where

$$\begin{aligned} x_k &= (t_n - t_0)(1 - e^{-x_k^*}) + t_0, \\ w_k &= (t_n - t_0)^{1-\alpha} (1 - x_k)^{-\alpha} w_k^*. \end{aligned} \quad (19)$$

The variables x_k^* and w_k^* correspond to the typical nodes and weights for Gauss–Laguerre quadrature, respectively, and the $1 - e^{-x_k^*}$ operation maps the nodes from $[0, \infty]$ to $[0, 1]$. This mapping is demonstrated in Figure 2. Note that there is a clustering of Gauss–Laguerre quadrature nodes near the singularity at the end of the interval.

Under appropriate conditions, this method is a viable means for approximating equation (7). However, the Gauss–Laguerre quadrature often requires extended numerical precision to achieve reasonably accurate results. This will be discussed further in Section 3.5, where we compare using this approach with and without extended numerical precision.

3.4. Hybrid quadrature methods

The two quadrature methods detailed previously provide reasonably accurate approximations for equation (7); however, each has specific limitations. The Riemann–Sum approach is extremely efficient since it does not require extended precision, but a potentially dense grid is required to maintain the assumption of a

piecewise constant function $f(t)$. In contrast, the Gauss–Laguerre method can provide reasonable approximations with fewer terms, with the notable exception that extended precision is required to achieve accurate estimates.

The main features of these quadrature methods is their ability to account for boundary singularities. Therefore, we propose a hybrid quadrature method that utilizes a more efficient approach in regions sufficiently far from the singularity. For example, Gauss–Legendre quadrature is an optimal approach for many integrals. Gauss–Legendre methods are not intended to be used to approximate integrals with boundary singularities; however, there is no reason why it cannot be utilized for the first part of the domain in equation (10). Mathematically, we observe that we can break the integral expression in equation (10) into two distinct components,

$$\int_{t_0}^t \frac{f(s)}{(t-s)^\alpha} ds = \underbrace{\int_{t_0}^{\delta} \frac{f(s)}{(t-s)^\alpha} ds}_{R1} + \underbrace{\int_{\delta}^t \frac{f(s)}{(t-s)^\alpha} ds}_{R2}. \quad (20)$$

An efficient quadrature method, such as Gauss–Legendre, can be utilized in R1 as long as a threshold value $\delta = \phi(t - t_0)$ maintains sufficient distance from the singularity. The remaining portion of the integral R2 can be approximated using one of our more specialized methods, Riemann–Sum or Gauss–Laguerre. One adjusts how the domain is partitioned by specifying different values of ϕ . Details regarding the hybrid methods employed in this work, such as Gauss–Legendre, Riemann–Sum or Gauss–Laguerre, Gauss–Laguerre may be found in Miles et al. (2018).

3.5. Convergence of quadrature methods

To properly assess the viability of these numerical methods, we will compare their performance on several test problems. We first consider the fractional derivative of two simple functions: (1) $f(t) = \exp(2t)$ and (2) $f(t) = \cos(2t)$. Furthermore, we will consider the fractional derivative of these functions at several different points in time. The reference solutions for each test problem were calculated using Mathematica (Wolfram Research, Inc., 2018). The numerical implementations can be found in the Python package pyfod (Miles and Pash, 2019). The convergence trends presented in Figure 3 appear to be approximately linear with respect to the number of quadrature nodes in log–log space, which is not surprising. Utilizing the hybrid quadrature approach with Gauss–Legendre and Riemann–Sum enables one to expend more computational effort in the region near the singularity. Depending on the accuracy requirements, using just a few Riemann–Sum terms near the singularity can provide reasonable results.

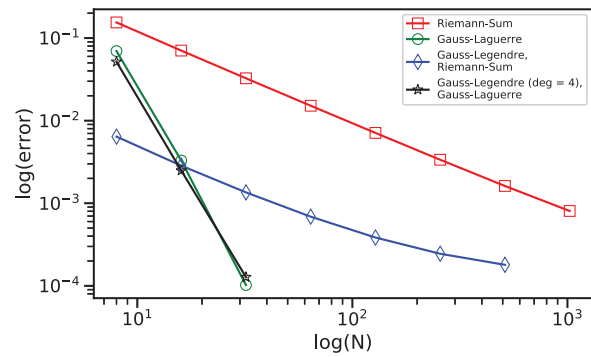


Figure 3. Relative error versus number of nodes for various quadrature methods for the test problem $f(t) = \exp(2t)$.

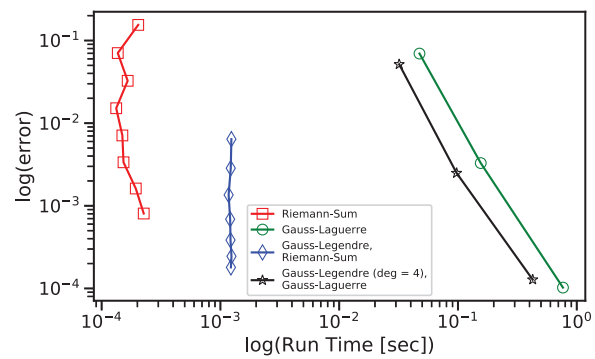


Figure 4. Relative error versus compute time for various quadrature methods for the test problem $f(t) = \exp(2t)$.

Often one is more constrained by evaluation time than storage to perform the computation. We present the computation times for the various methods in Figure 4. Note that run time requirements for the methods that use Gauss–Laguerre are significantly longer due to the use of symbolic expressions and extended precision. The trends presented in Figures 3 and 4 also hold for the test problem $f(t) = \cos(2t)$ as well as at various evaluation times and fractional-orders in $[0, 1]$.

One additional factor to account for when employing hybrid-quadrature methods is the choice of the threshold value ϕ that partitions the integration domain. In general it is desirable for ϕ to be large, so as to use an efficient quadrature scheme on the majority of the interval. However, this must be balanced with a degradation in performance if an inappropriate scheme is used near the boundary singularity. We investigate the effect of the ϕ on three test problems: $f(t) = \exp(2t)$, $\cos(2t)$, $t^2 - t + 1$ on the domain $[0, 1]$ with $\alpha = 0.9$ using the Gauss–Legendre, Riemann–Sum hybrid method. The results of this study are presented in Figure 5.

The trends in Figure 5 demonstrate the phenomenon that when ϕ is chosen so that the Gauss–Legendre domain of integration approaches the singularity,

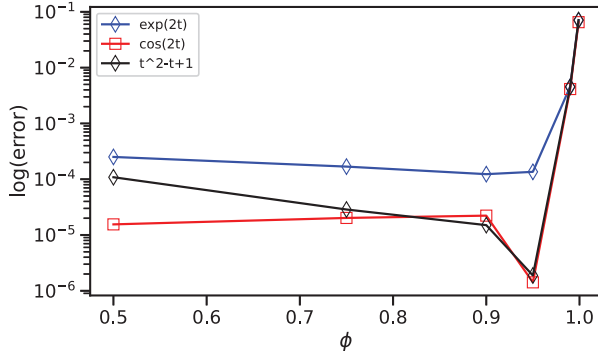


Figure 5. Relative error versus ϕ for various quadrature methods for the test problems $f(t) = \exp(2t)$, $\cos(2t)$, $t^2 - t + 1$ on domain $[0, 1]$ with $\alpha = 0.9$.

performance begins to drastically degrade. Conversely, when ϕ is too small, then many of the benefits of using a more efficient quadrature are lost. As a heuristic, the authors recommend and employ a selection of $\phi = 0.95$ that represents a 95%/5% partition of the integration domain.

3.6. Reference solution

In many cases, a reference solution cannot be analytically or symbolically determined, such as for the viscoelastic model. Thus, we consider the Grünwald–Letnikov (*GLet*) fractional derivative to be our reference given its general acceptance in literature. Since we are primarily interested in testing our numerical methods ability to achieve accuracy to the first decimal place, we run our reference solution until it has converged up to the second decimal place in accuracy. Mathematically, we compare increased levels of grid density at certain reference points until the residuals satisfy variation in only the third decimal place; that is,

$$\|x_{k+1}^{GLet} - x_k^{GLet}\|_{\infty} \leq 10^{-2}. \quad (21)$$

Note that k refers to the level of grid resolution, so $k + 1$ is a more refined grid, that is more nodes than k . When comparing the overall accuracy of our other numerical methods, we will consider their ability to achieve accuracy to the second decimal place with respect to the reference solution found using the Grünwald–Letnikov definition. We can express this as

$$\|x_{ref}^{GLet} - x_k^i\|_{\infty} \leq 10^{-1}, \quad (22)$$

where i refers to one of our numerical methods; for example, Riemann–Sum (RS) or Gauss–Laguerre (GL), and k is the grid level being tested.

3.7. Convergence of viscoelastic model

When using our nonlinear viscoelastic model in studies that require numerous model evaluations, such as

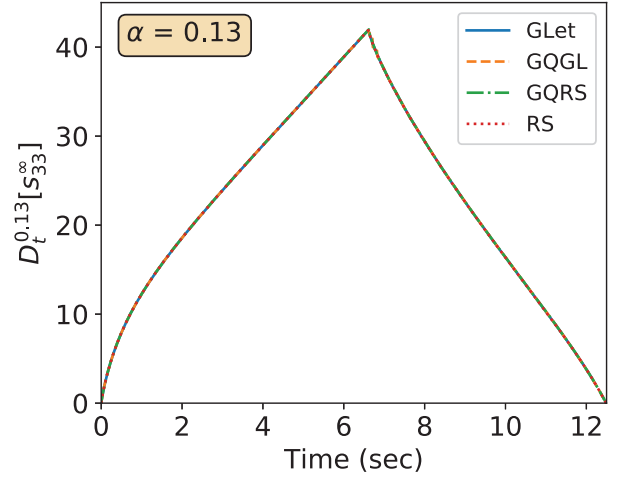


Figure 6. Operator comparison with small fractional order, α .

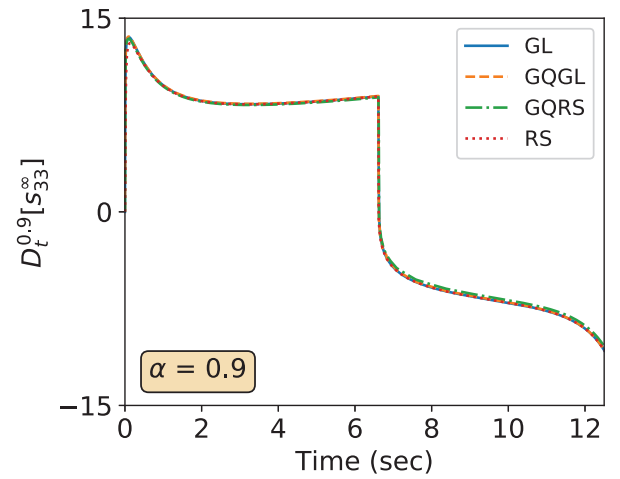


Figure 7. Operator comparison with large fractional order, α .

Bayesian inference, we are concerned with the trade-off between numerical fidelity and computational speed. Moreover, the model response is highly dependent on fractional-order. Figures 6 and 7 show that the numerical methods converge to similar estimates of the fractional derivative for both small and large fractional-orders, α . Additionally, we can look at convergence of the various operators with respect to the reference solution in the ℓ_2 and ℓ_{∞} norms as in Figures 8 and 9. Similar to the results from Section 3.5, we note that the hybrid Gauss–Legendre and Riemann Sum (GQRS) method achieves a good trade-off between accuracy and computational efficiency. Moreover, we have demonstrated that our quadrature schemes converge to the desired level of accuracy (L_{∞} – norm $\leq 10^{-1}$) with regard to the fractional-order derivative operation.

4. Experimental data

To perform model calibration, we consider the set of experiments performed in Miles et al. (2015). The

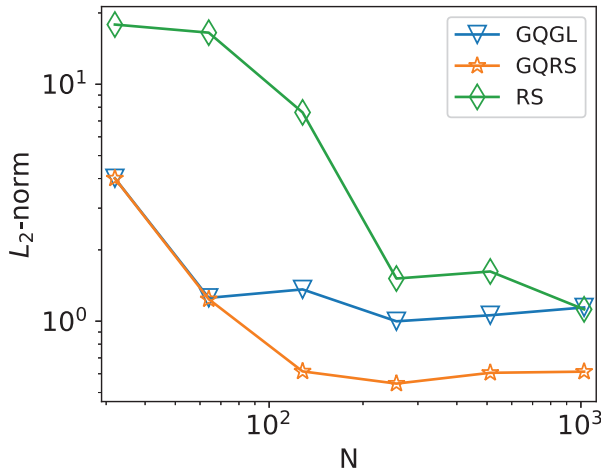


Figure 8. Operator convergence in L_2 -norm.

reader is referred to that paper for more details, but the key components of the experimental procedure are outlined below.

A series of uni-axial, cyclic loading experiments were performed on the elastomer Very High Bond (VHB) 4910 (made by 3M). Each experiment consisted of stretching the specimen a fixed amount at a specified rate, then returning the specimen to its original length at the same rate. This deformation cycle was repeated 12 times in order to reach steady-state hysteresis. The experiments were varied by performing the same deformation sequence but at different deformation rates. In this manner, a set of data highlighting the rate-dependent qualities of VHB 4910 were collected. The raw data collected from the MTS Instron machine provides the load (L_{33} —assuming deformation in the x_3 -direction) for each deformation state. Using the nominal specimen dimensions (thickness and width) we compute the original cross-sectional area (A_0) and subsequently the nominal stress— $s_{33} = L_{33}/A_0$. For the purpose of model calibration, we compare our model to the nominal stress, steady-state hysteresis response achieved from the final cycle of each experiment.

5. Parameter subset selection

For our fractional-order nonlinear viscoelastic model, a primary objective is to infer distributions for the parameter set

$$\theta = [G_c, G_e, \lambda_{max}, \eta, \alpha, \gamma, \beta_\infty]. \quad (23)$$

Previous research has shown that the full set of model parameters may not be identifiable (Mashayekhi et al., 2018; Miles et al., 2015), in the sense that they are not uniquely determined by observed data. This motivates the need for sensitivity analysis to inform parameter selection. We use the parameter subset selection (PSS) algorithm as detailed in Leon et al. (2019). Details of

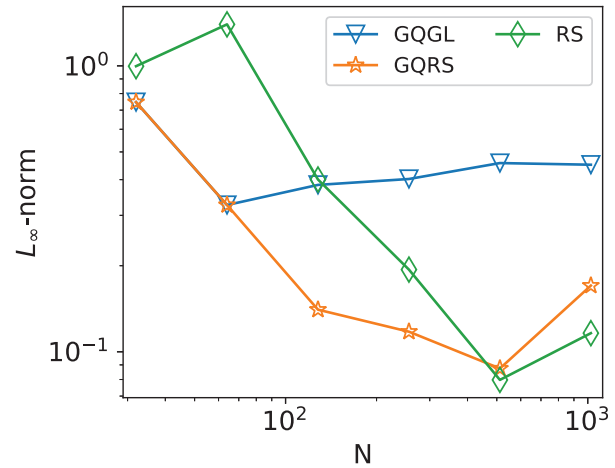


Figure 9. Operator convergence in L_∞ -norm.

this analysis were reported in Miles et al. (2019), but we include the conclusions here for clarity.

The goal of PSS is to reduce the number of parameters to those that are identifiable. This is accomplished by a systematic comparison of the eigenvalues of the Fisher Information matrix. Details of the algorithm can be found in Quaier and Mönnigmann (2009) and Leon et al. (2018). Consider the sensitivity matrix of the form

$$S = \begin{bmatrix} \frac{\partial f}{\partial \theta_1}(x_1^1; \theta^*) & \cdots & \frac{\partial f}{\partial \theta_p}(x_p^1; \theta^*) \\ \vdots & & \vdots \\ \frac{\partial f}{\partial \theta_1}(x_1^N; \theta^*) & \cdots & \frac{\partial f}{\partial \theta_p}(x_p^N; \theta^*) \end{bmatrix}, \quad (24)$$

where θ^* is a nominal set of parameter values, and f is the model for our quantity of interest (QoI). This matrix reflects a system with N independent points of evaluation, and p model parameters; $p = 7$ based on the set defined in equation (23). The nominal parameters were identified using a least-squares fit between the nominal-stress model outlined in Section 2 and a set of experimental observations, details of which are provided in Section 4. A summary of the nominal parameters identified by the least-squares fit are presented in Table 1.

Upon performing the PSS algorithm using the scaled Fisher information matrix $S^T S$, we observe the significant jump in relative eigenvalues between the 5th and 6th parameter, shown in Figure 10. This indicates that five of the model parameters are significantly more influential in impacting the QoI. We determine the corresponding non-influential parameters by finding the smallest relative eigenvalue, and then identifying the largest magnitude eigenvector component. This eigenvector component corresponds to a specific parameter. This process is repeated iteratively by removing the column and row corresponding to the non-influential

Table 1. Nominal model parameters identified from least-squares fit.

Parameter	Units	Nominal value
G_c	kPa	5.01
G_e	kPa	0.82
λ_{max}	—	9.24
η	—	1060
α	—	0.165
γ	—	2720
β_∞	—	2.07

parameter in the sensitivity matrix, then reassessing the relative eigenvalue spectrum. From the iteration results presented in Table 2, we conclude that the parameters γ and η are non-influential and use their nominal values identified from the least-squares fit for subsequent model evaluation and calibration. With this information, we consider the parameter set

$$\theta = [G_c, G_e, \lambda_{max}, \beta_\infty, \alpha].$$

6. Bayesian model calibration

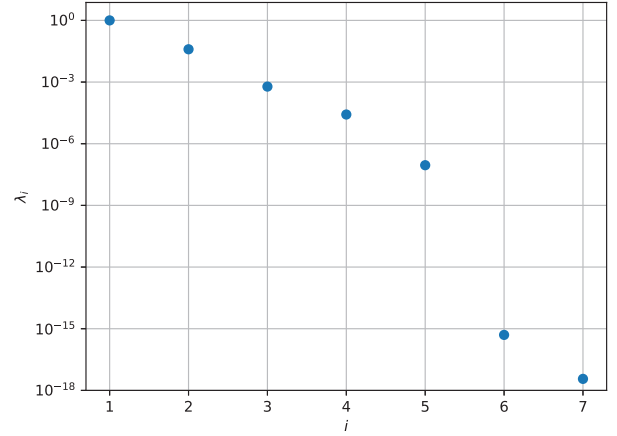
With an efficient model representation and a set of sensitive parameters, we now infer the model parameters in the presence of observation uncertainty. As detailed in (Smith, 2014) this is natural in a Bayesian framework. The basic objective of Bayesian inference is to construct the model parameter posterior densities given some set of observations. This can be expressed using Bayes' relation

$$\pi(\theta|M^{data}) = \frac{\pi(M^{data}|\theta)\pi_0(\theta)}{\int_{\mathbb{R}^1} \pi(M^{data}|\theta)\pi_0(\theta)d\theta}. \quad (25)$$

We assume a statistical model of the form

$$M^{data} = M(x_i; \theta) + \varepsilon_i. \quad (26)$$

Here $M(x_i, \theta)$ represents our model generating observations at x_i with model parameters θ . This form assumes the observation errors are independent and identically distributed (iid); that is, $\varepsilon_i \stackrel{iid.}{\sim} \mathcal{N}(0, \sigma^2)$. A

**Figure 10.** Eigenvalues from first iteration of PSS algorithm using quasi-global sensitivity matrix.

direct result of this formulation is that the likelihood function is

$$\pi(M^{data}|\theta) = e^{-SS_q/(2\sigma^2)} \quad (27)$$

where $SS_q = \sum_{i=1}^D [M^{data}(i) - M(x_i; \theta)]^2$ is the sum-of-squares error, where D is the number of observations. Any *a priori* information about the model parameters is defined in the prior function, $\pi_0(\theta)$. So as not to bias the sampling procedure, we assume a flat prior distribution for all parameters.

Direct evaluation of Bayes' relation is untenable for most problems due to having to integrate in \mathbb{R}^p . Instead, we use Markov Chain Monte Carlo (MCMC) methods. For this problem, we use the MCMC implementation available in the Python package pymcmcstat (Miles, 2019). For sampling, we use the Delayed Rejection Adaptive Metropolis (DRAM) algorithm (Haario et al., 2006). Here we calibrate our model of the nominal stress equation (4) with respect to two experimental data sets together to infer a single set of posterior densities. From a set of experiments described in Miles et al. (2015), we choose the data from the slowest and fastest stretch rates. Each data set is assumed to have different error variances as the amount of noise may differ between experiments.

Table 2. Results from performing parameter subset selection with the quasi-global sensitivity matrix to determine noninfluential parameters in θ .

Eigenvector $\Delta\theta_1$ with corresponding parameters								
Iteration	$ \lambda_1 $	G_c	G_e	λ_{max}	η	γ	β_∞	α
1	3.60e-19	-1.67e-03	-2.72e-04	-9.82e-08	5.25e-01	8.51e-01	1.03e-03	-5.17e-09
2	2.32e-16	-8.54e-03	-1.39e-03	-2.97e-06	9.99e-01	—	5.30e-03	-5.80e-07
3	8.94e-08	7.90e-01	7.90e-02	1.17e-01	—	—	-5.97e-01	-5.12e-03
4	2.68e-05	—	3.50e-01	-9.28e-01	—	—	-1.27e-01	-6.81e-04

Result: The parameters γ and η are not influential.

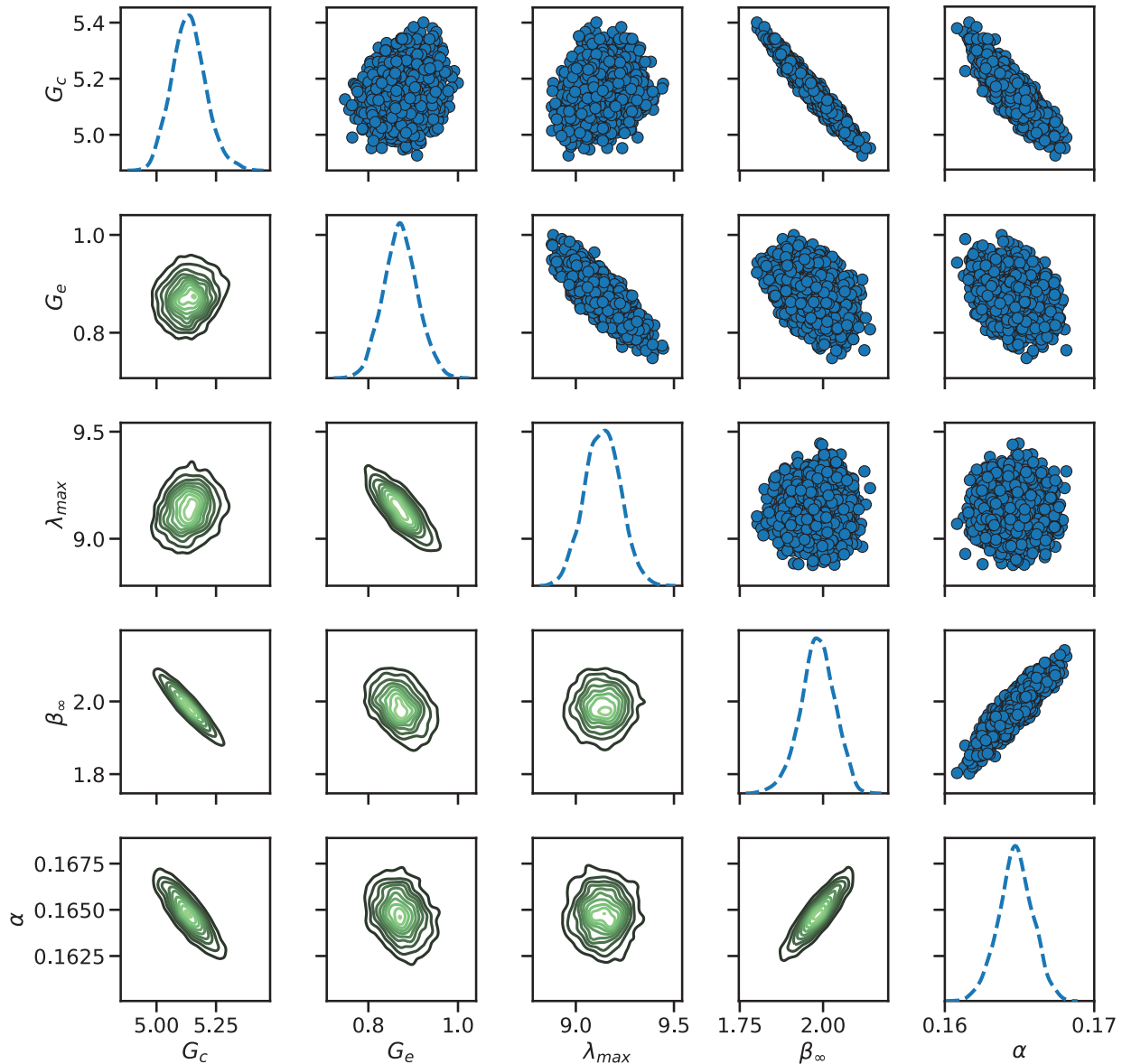


Figure 11. (Main Diagonal) Marginal posterior densities, (Lower Triangular) joint kernel density estimates, and (Upper Triangular) pairwise correlations.

From the results of the sensitivity analysis reported in Section 5, the calibration parameter set is

$$\theta_{DRAM} = [G_c, G_e, \lambda_{max}, \beta_{\infty}, \alpha]. \quad (28)$$

DRAM is used for calibration with 100,000 samples, of which the first half are considered to be the “burn-in” period, where the chains are exploring the space and the posteriors are converging. We present results of this calibration in Figure 11. We note the unimodal appearance of the kernel density estimate (KDE) of the marginal posterior densities on the main diagonal of Figure 11. This is not required for our purposes, but it is noted that a Q-Q plot could be used to determine if the posteriors are normally distributed.

Additionally, the calibration process allows us to visualize parameter correlations as shown in the off-diagonals of Figure 11. In the upper-diagonal, we observe pairwise MCMC samples and in the lower-diagonal we see the corresponding joint distribution estimate. The upper- and lower-diagonal plots present parameter correlation, but some readers may find one representation more intuitive to understand than the other. Figure 11 reveals correlation structure among many of the parameters. A somewhat linear correlation is observed between the parameter sets $[\alpha, \beta_{\infty}]$, $[\alpha, G_c]$, $[G_c, \beta_{\infty}]$, and possibly $[G_e, \lambda_{max}]$. It is not surprising to see correlated parameters in our calibration as the different components of the model interact with each other. This is true for the viscoelastic parameters and

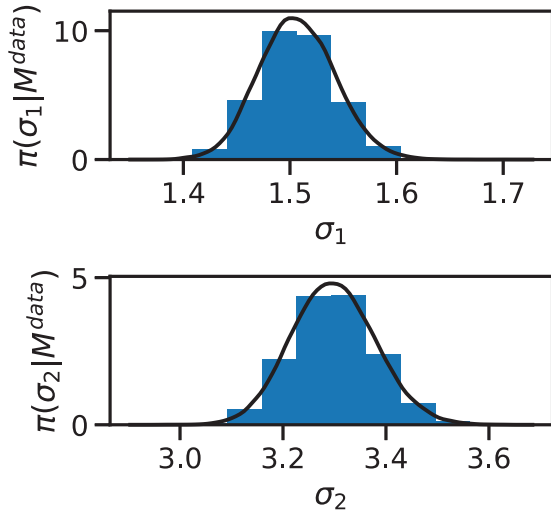


Figure 12. Posterior estimates of measurement variance for both data sets used for calibration.

hyperelastic parameters as each parameter can influence the stress state but in a different manner. For example, the crosslink modulus, G_c depends on the network crosslinking density while the entanglement modulus, G_e , depends more strongly on neighboring monomer interactions. It is also not surprising to see positive correlations between the fractional viscoelastic order α and β_∞ which weights the viscoelastic stress. The MCMC approach to calibration works well when dealing with correlated parameters, and these results support the conclusion from Section 5 that we are calibrating an identifiable subset. If these correlation structures were extremely tight (i.e., a completely straight line), then that would imply a single-value correlation, which means one parameter can be directly defined from the value of another. If that were the case, then the parameters would not be uniquely identifiable, and we would need to re-address the results of the sensitivity analysis. Furthermore, we note that the parameter distributions are similar to those presented in Mashayekhi et al. (2018) and Miles et al. (2015). Additionally, the variance estimates for the two data sets used for calibration support our assumption that each data set has unique measurement errors. As seen in Figure 12, the measurement error for the fastest stretch rate (σ_2) has a broader distribution with a larger mean value. This is not surprising as we expect more sources of uncertainty or noise to exist in the experiment when deforming the specimen at a faster rate.

We now employ the posterior parameter distributions to evaluate model performance across stretch rates by propagating the uncertainty through the model. The results for the slowest and fastest stretch rates are co-plotted in Figure 13. We note that the fractional-order model is able to effectively quantify

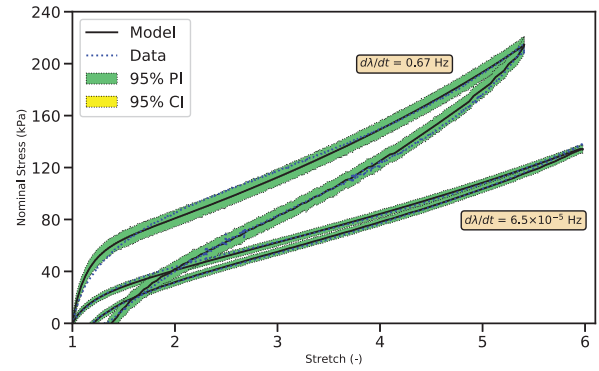


Figure 13. Uncertainty propagation with non-linear fractional-order viscoelastic model at slowest and fastest stretch rates.

the stress response of the material at both stretch-rates and that the experimental data is entirely encapsulated within our 95% prediction intervals. Prediction intervals are the sum of propagated parameter uncertainties and measurement uncertainty, and estimate the region where new data measurements would be expected to be. We note the tight intervals in Figure 13 are useful for predictive estimation. For more details regarding the interpretation of credible and prediction intervals, the reader is referred to Smith (2014).

7. Conclusion

In this paper, we have outlined the development of a nonlinear fractional-order viscoelastic modeling framework for soft dielectric elastomers. We then introduce the Riemann-Liouville definition of the fractional derivative and the development of various quadrature methods, including hybrid methods to compute the fractional derivative. Convergence tests of the quadrature methods indicate that the hybrid Gauss-Legendre, Riemann-Sum method offers a good trade-off between convergence speed and computational efficiency. Moreover, we have demonstrated the ability of all of the methods to converge for the nonlinear viscoelastic model presented in Section 2.

We have also shown how parameter subset selection can be used to identify the most sensitive model parameters and reduce the calibration set from seven to five parameters by fixing γ and η . MCMC calibration results support the conclusion that the parameters in equation (28) are all significant and identifiable. Moreover, once calibrated, the nonlinear fractional-order model shows good agreement with experiments at multiple stretch rates with the data completely contained in the prediction intervals.

The fractional viscoelastic order found from the reduced calibration set was nominally 0.165. This result is self-consistent with prior Bayesian parameter

calibration of the full parameter set (Mashayekhi et al., 2018). While α is significantly lower than 1 (conventional dashpot model), the results given here provide accurate viscoelastic prediction over a relatively large strain rate range, as discussed elsewhere (Mashayekhi et al., 2018). This is believed to be a consequence of the non-local fractional order derivative. Its complexity has also been shown to be related to fractal geometry and power-law spectral dimensions of the underlying polymer dynamics (Mashayekhi et al., 2019) which offers additional opportunities to understand complex multiscale effects associated with nonlinear mechanics in soft materials.


Declaration of conflicting interests


The author(s) declared no potential conflicts of interest with respect to the research, authorship, and/or publication of this article.

Funding

The author(s) disclosed receipt of the following financial support for the research, authorship, and/or publication of this article: The research of PRM and RCS was supported in part by the NSF Grant CMMI-1306290 Collaborative Research CDS&E and the Air Force Office of Scientific Research (AFOSR) grant FA9550-15-1-0299. The research of GTP was supported in part by the NSF grant DMS-1745654. The research of WSO was supported in part by the NSF Grant CMMI-1306320 Collaborative Research CDS&E.

ORCID iDs

Paul R Miles  <https://orcid.org/0000-0002-7501-5114>

Ralph C Smith  <https://orcid.org/0000-0001-7434-5712>

References

- Atangana A and Gómez-Aguilar J (2018) Numerical approximation of riemann-liouville definition of fractional derivative: From riemann-liouville to atangana-baleanu. *Numerical Methods for Partial Differential Equations* 34(5): 1502–1523.
- Davidson JD and Goulbourne N (2013) A nonaffine network model for elastomers undergoing finite deformations. *Journal of the Mechanics and Physics of Solids* 61(8): 1784–1797.
- Griebel M and Oettershagen J (2014) Dimension-adaptive sparse grid quadrature for integrals with boundary singularities. In: Garcke J and Plüger D (eds) *Sparse Grids and Applications-Munich 2012*. Cham: Springer, pp.109–136.
- Haario H, Laine M, Mira A, et al. (2006) DRAM: Efficient adaptive MCMC. *Statistics and computing* 16(4): 339–354.
- Holzappel GA (2000) *Nonlinear Solid Mechanics*, vol. 24. Chichester: John Wiley & Sons.
- Holzappel GA and Simo JC (1996) A new viscoelastic constitutive model for continuous media at finite thermomechanical changes. *International Journal of Solids and Structures* 33(20–22): 3019–3034.
- Leon L, Smith RC, Oates WS, et al. (2018) Analysis of a multi-axial quantum-informed ferroelectric continuum model: Part 2 – sensitivity analysis. *Journal of Intelligent Material Systems and Structures* 29(13): 2840–2860.
- Leon LS, Miles PR, Smith RC, et al. (2019) Active subspace analysis and uncertainty quantification for a polydomain ferroelectric phase-field model. *Journal of Intelligent Material Systems and Structures* 30(14): 2027–2051.
- Mashayekhi S, Hussaini MY and Oates W (2019) A physical interpretation of fractional viscoelasticity based on the fractal structure of media: Theory and experimental validation. *Journal of the Mechanics and Physics of Solids* 128: 137–150.
- Mashayekhi S, Miles P, Hussaini MY, et al. (2018) Fractional viscoelasticity in fractal and non-fractal media: Theory, experimental validation, and uncertainty analysis. *Journal of the Mechanics and Physics of Solids* 111: 134–156.
- Miles P, Hays M, Smith R, et al. (2015) Bayesian uncertainty analysis of finite deformation viscoelasticity. *Mechanics of Materials* 91: 35–49.
- Miles P and Pash G (2019) pyfod. Version 0.1.0. Zenodo.
- Miles P, Pash G, Oates W, et al. (2018) Numerical techniques to model fractional-order nonlinear viscoelasticity in soft elastomers. In: *ASME 2018 conference on smart materials, adaptive structures and intelligent systems*, San Antonio, TX, 10–12 September 2018, vol. 51944, p.V001T03A021. American Society of Mechanical Engineers.
- Miles PR (2019) A python package for bayesian inference using delayed rejection adaptive metropolis. *Journal of Open Source Software* 4(38): 1417.
- Miles PR, Pash GT, Smith RC, et al (2019) Global sensitivity analysis of fractional-order viscoelasticity models. In: *Behavior and mechanics of multifunctional materials XIII*, Denver, Colorado, 29 March 2019, vol. 10968, p.1096806. International Society for Optics and Photonics.
- Oldham K and Spanier J (1974) *The Fractional Calculus Theory and Applications of Differentiation and Integration to Arbitrary Order*, vol. 111. New York and London: Academic Press.
- Podlubny I (1998) *Fractional Differential Equations: An Introduction to Fractional Derivatives, Fractional Differential Equations, to Methods of Their Solution and Some of Their Applications*, vol. 198. San Diego, US: Academic press.
- Quaiser T and Mönnigmann M (2009) Systematic identifiability testing for unambiguous mechanistic modeling–application to JAK-STAT, MAP kinase, and nf- κ B signaling pathway models. *BMC Systems Biology* 3(1): 50.
- Smith RC (2014) *Uncertainty quantification: Theory, implementation, and applications*, vol. 12. Philadelphia, PA: SIAM.
- Wolfram Research Inc (2018) Mathematica, Version 11.3. Champaign, IL.